

# How cell design affects the performance of sodium-antimony-bismuth liquid metal batteries

Renate Fetzter<sup>\*</sup>, Tianru Zhang, Florian Lindner, Alfons Weisenburger, Georg Müller

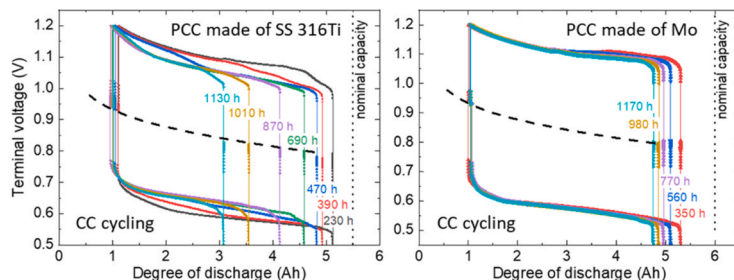
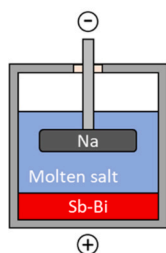
Institute for Pulsed Power and Microwave Technology (IHM), Karlsruhe Institute of Technology (KIT), Hermann-von-Helmholtz-Platz 1, 76344, Eggenstein-Leopoldshafen, Germany

## HIGHLIGHTS

- Na/SbBi<sub>9</sub> liquid metal batteries with different cell designs operate successfully.
- Cells show excellent cycling performance with only 0.35 mA/cm<sup>2</sup> self-discharge.
- Long-term operation shows capacity decrease due to Na evaporation and corrosion.
- Corrosion effects are avoided when Mo is used as positive current collector.

## GRAPHICAL ABSTRACT

### Na-LMB



## ARTICLE INFO

### Keywords:

Liquid metal battery (LMB)  
Sodium  
Sb-Bi alloy  
Electrochemical performance  
Capacity loss  
Corrosion

## ABSTRACT

Low-cost sodium-based liquid metal batteries are attractive candidates for grid-scale stationary energy storage. In this study, the performance of Na/SbBi<sub>9</sub> test cells with molten salt electrolyte LiCl-NaCl-KCl (61-3-36 mol%) is evaluated for different cell designs. Cells with a metal foam hosting the negative electrode (5–6 Ah nominal capacity) and cells without foam are investigated. Additionally, the amount of electrolyte and the material used as positive current collector (PCC) are varied. The self-discharge current is only  $\sim 0.35$  mA/cm<sup>2</sup> and depends reasonably on electrode distance and operating temperature. Contact resistances are 10 m $\Omega$  in total and thus smaller than the ohmic resistance of the electrolyte. The cell voltage is not affected by cell design, operating temperature, or cell age. Long-term cycling tests show a capacity decrease, which can be attributed to evaporation of Na. An additional capacity loss observed in cells with stainless steel PCC can be avoided by using Mo as PCC.

## 1. Introduction

Liquid metal batteries (LMBs) are researched as potential large-scale stationary energy storage systems to compensate the intermittence of renewable energy sources and to stabilize the power grids [1,2]. LMBs

are comprised of two liquid metal electrodes and a molten salt electrolyte, which stay separated due to density differences and mutual immiscibility. Upon discharging, the low-density, low-electronegativity metal of the negative electrode is oxidized and its ions are conducted via the electrolyte to the positive electrode, where they are reduced and

<sup>\*</sup> Corresponding author.

E-mail address: [renate.fetzter@kit.edu](mailto:renate.fetzter@kit.edu) (R. Fetzter).

alloyed with the high-density, high-electronegativity metal of the positive electrode. The described processes are reversed upon charging. Due to the all-liquid nature of electrodes and electrolyte, no degradation of active materials occurs upon cycling, promising a long service life. In addition, the fast reaction kinetics at the electrode-electrolyte interfaces allows high current densities. Low-cost, simple assembly, and easy scalability complement the advantages of LMBs.

Despite the great progress and excellent electrochemical performance of lithium as negative electrode material in lithium-ion batteries and Li-based LMBs [3–5], Li is not an abundant element and there are considerable concerns about environmental issues and increasing costs of the exploitation of Li-containing minerals. Regarding magnesium and calcium as negative electrode [6,7], both possess relatively high melting points (650 °C for Mg, 842 °C for Ca). The unavoidably high cell operating temperature brings technical challenges, increases the metal solubility in the molten salt electrolyte and, thus, the self-discharge of the cell, enhances corrosion issues on structural materials, and limits the service life.

Due to the high abundance and low melting temperature of sodium (Na), Na-based LMBs have environmental and economic advantages over LMBs using other metals as negative electrode. However, the high melting temperature of Na halide salts (e.g., ~530 °C for NaF–NaCl–NaI) results in high operating temperatures, a high Na solubility in the molten salt electrolyte (~4 mol% for NaF–NaCl–NaI) and substantial self-discharge of the cells [1,8]. In recent years, intense research on various molten salt systems was performed to find an appropriate electrolyte for Na-LMBs that combines a low melting temperature and a low Na solubility with a still acceptable  $\text{Na}^+$  conductivity. The multi-cationic salt system LiCl–NaCl–KCl in its eutectic composition with less than 9 mol% NaCl was found to fulfil these requirements [9, 10]. The melting temperature is reduced to ~350 °C and the solubility of Na metal is reduced to ~0.4 mol%. The suitability of the molten salt system LiCl–NaCl–KCl as electrolyte in Na-LMB cells could be demonstrated in test cells with 1 Ah and 10 Ah nominal capacity [10].

Antimony (Sb) is regarded as the most promising positive electrode material for LMBs owing to its low cost and high cell voltage. Its high melting temperature of 631 °C is typically reduced by alloying with lead, tin, or bismuth without a significant decrease in cell voltage [3,4]. Because of the environmental concerns of large-scale application of lead and the corrosion issues introduced by the use of tin [11–14], bismuth remains as a feasible option [5,15].

In the current study, various Na-LMB cells with the molten salt LiCl–NaCl–KCl (61-3-36 mol%) as electrolyte and SbBi<sub>9</sub> alloy as positive electrode were built and tested. In addition to demonstrating the excellent performance of the hermetically closed test cells, the influence of the specific cell design on different electrochemical parameters was systematically investigated. The liquid Na was either hosted by a metal foam, which fixed the nominal capacity to 5–6 Ah, or floated freely on top of the electrolyte, allowing to achieve higher cell capacities. For both cell designs, the cell voltage, self-discharge current, and ohmic cell

resistance were quantified as function of the distance between the electrodes and of the operating temperature. The long-term electrochemical performance was investigated and the influence of the amount of electrolyte and of the material chosen as positive current collector was assessed.

## 2. Materials and Methods

### 2.1. Cell design and assembly

Fig. 1 shows the design of the investigated Na-LMB test cells. The cell body of the cells is made of stainless steel 316Ti and serves as positive current collector. It is filled with the positive electrode alloy SbBi<sub>9</sub> and the molten salt electrolyte LiCl–NaCl–KCl (61-3-36 mol%). The inner diameter of the cell body is 60 mm. An amount of 130 g of SbBi<sub>9</sub> (0.065 mol Sb, 0.585 mol Bi) is chosen to obtain a positive electrode with thickness 5 mm. The negative electrode Na is hosted by a Ni foam (porosity 50 PPI, diameter 50 mm, thickness 5 mm), which can adsorb about 5 g of Na (0.2 mol) and is fixed to a foam holder (shown in blue in Fig. 1(b)) with Mo wires. The distance between the electrodes is adjusted to values typically between 11 and 14 mm. The amount of electrolyte (at least 120 g) suffices to fully cover the negative electrode including the foam holder. The negative current collector holds the Ni foam and connects the negative electrode with the outer circuit. It is insulated from the cell body by a gas-tight sealing.

The Na-LMB cells were assembled in a glovebox with controlled Ar atmosphere ( $\text{O}_2 < 1$  ppm,  $\text{H}_2\text{O} < 0.5$  ppm) to avoid moisture and oxygen impurities inside the cell. Prior to assembly, the individual components were prepared and purified as described in the following.

To prepare the SbBi<sub>9</sub> alloy for the positive electrode, antimony and bismuth (both: purity 99.99 %, HHW Haunder GmbH & Co. KG) were mixed in their granular forms in the appropriate ratio in an alumina crucible and melted in an oxygen-free atmosphere. The alloy was kept for 2 h at 700 °C in reducing atmosphere generated by an Ar5% $\text{H}_2$  gas flow to remove all remaining oxides. After cooling down, the crucible with the solidified alloy was transported immediately into the glovebox, where the alloy was melted again and poured into the cell body.

For the negative electrode, sodium blocks (purity 99.8 %, Haines & Maassen Metallhandelsgesellschaft GmbH) were melted and further purified inside the glovebox in a specially designed sodium sink heated to 130 °C. In order to achieve penetration of Na into the pores of the Ni foam, liquid sodium was poured in a glass container and the foam was submerged into the Na. Then, the glass container was set under vacuum to force liquid sodium into the pores. The amount of adsorbed Na was determined for each foam/cell. It was in the range 4.2–5.1 g (0.18–0.22 mol), which translates into a nominal cell capacity  $Q_{nom}$  in the range 4.9–6.0 Ah. Note that the rather high amount of Sb–Bi alloy (0.65 mol) does not limit the cell capacity. After cooling to room temperature, the Na-containing foam was fixed to the foam holder using Mo wires.

Preparation of the electrolyte also took place directly in the glove-

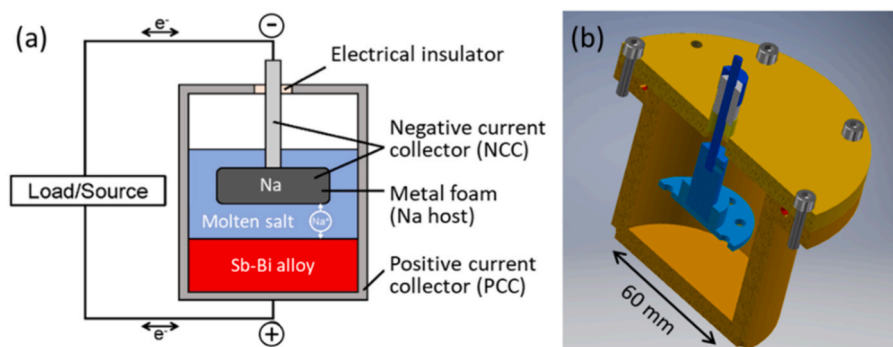


Fig. 1. Design of Na-LMB test cells: (a) schematic including active liquid components, (b) design (to-scale) of solid components.

box. The salts LiCl (anhydrous, purity 99.9 %, Apollo Scientific), NaCl (anhydrous, free-flowing, purity  $\geq 99.0$  %, Honeywell), and KCl (purity  $\geq 99.5$  %, Sigma-Aldrich) were mixed in the appropriate ratio in a stainless-steel container and heated to 150 °C and 300 °C for 30 min each to remove remaining moisture. Then the salt mixture was melted at 600 °C and poured into the cell body, which already contained the Sb–Bi alloy. With the salt still molten, the negative electrode was added and the cell body was hermetically closed. Thus, no further exchange with the atmosphere around the cell took place.

Some cells were assembled without the metal foam hosting the sodium. Instead, a ceramic sheath was introduced to insulate the liquid sodium floating freely on top of the molten salt from the side walls of the cell case. The ceramic sheath reduced the cell's inner diameter to 48 mm. In this foam-less design, the amount of salt was reduced to 90 g, the distance between the electrodes was around 22 mm, and the amount of Na was 20–30 g.

The assembled cells were labelled according to their design with D1, D2, etc. for the default design and with FL1, FL2 for the foam-less design.

To operate the cells, they were put in heating sleeves and heated from below to a specific set temperature. Although the heating sleeves containing the cells were insulated to the side and covered by ceramic plates to improve thermal insulation to the top, a temperature gradient existed inside the cells with the coldest part being the cell cover. For a set temperature of 500 °C below the cell, the positive electrode was found to attain a temperature of  $\sim 435$  °C, the electrolyte  $\sim 430$  °C, and the vapor close to the cell cover  $\sim 350$  °C.

## 2.2. Electrochemical tests

Various electrochemical tests were performed by a high-current Arbin electrochemical station (LBT21084HC). For galvanostatic cycling with potential limitation (GCPL), the cells were charged and discharged at constant current (typically  $\pm 100$  mA/cm<sup>2</sup> or  $\pm 200$  mA/cm<sup>2</sup>, normalized to the surface of the positive electrode) to specific fixed voltage limits and the voltage response was recorded. Each charging/discharging step was followed by a short relaxation step (typically 1–5 min) at zero current. Different current densities up to  $\pm 600$  mA/cm<sup>2</sup> were used for charge-discharge cycling in order to determine the rate capability of the cells. Long-term cycling tests were performed to characterize the cell stability.

For each charge-discharge cycle, the charge capacity  $Q_{ch}$  and the discharge capacity  $Q_{disc}$  were determined by integrating the charge respectively discharge current (its absolute value) over the cycle duration,  $Q_{ch/disc} = \int |I_{ch/disc}(t)| dt$ . The ratio of both quantities,  $Q_{disc}/Q_{ch}$ , is defined as Coulombic efficiency. From the difference between charge and discharge capacity, the average self-discharge current  $I_{sd}$  of the cell was determined,  $\int I_{sd}(t) dt = Q_{ch} - Q_{disc}$ .

The charge and discharge energies of each charge-discharge cycle are given by  $E_{ch/disc} = \int U_t(t) \bullet |I_{ch/disc}(t)| dt$ , where  $U_t(t)$  is the measured terminal voltage. The ratio  $E_{disc}/E_{ch}$  is defined as energy efficiency and is strongly influenced by the overpotentials  $\eta_i$ , which determine the difference between the measured terminal voltage  $U_t$  and the cell voltage  $U_0$  according to  $U_t = U_0 + \sum_i \eta_i$ . Typical overpotentials of LMB cells are the ohmic overpotential, the activation overpotential, and the mass transport overpotential. Throughout this paper, the sign of the charging/discharging currents and overpotentials are chosen positive for charging and negative for discharging.

The galvanostatic intermittent titration technique (GITT) was used to determine the correlation between the static electrochemical cell voltage  $U_0$  and the molar Na concentration in the Na–Sb–Bi alloy of the positive electrode,  $x_{Na} = n_{Na}/(n_{Na} + n_{Sb} + n_{Bi})$ . A series of short pulses of constant current, each followed by an appropriate relaxation time, was applied to the test cells and the voltage response of the cells was measured. The relaxed voltage data after each titration step correspond to the cell voltage at the given state of charge  $SOC(t) = SOC_0 + \int I(t) dt$ .

## 3. Results and discussion

### 3.1. Cycling tests

Data of typical charge-discharge cycles (GCPL tests) with constant current (here  $\pm 2.83$  A, corresponding to  $\pm 100$  mA/cm<sup>2</sup>) are shown in Fig. 2(a) for a cell with default design. Upon switching on a constant positive (negative) current, the measured terminal voltage jumps (IR drop) and then further increases (decreases) as the cell is charged (discharged). When reaching the set voltage limit, the current is switched off and the terminal voltage jumps back by  $-IR$ , followed by relaxation of remaining overpotentials. Note that the lower voltage limit of 0.5 V was chosen low enough to obtain a quickly decreasing voltage at the end of the discharge process, which indicates that all available Na is oxidized to Na<sup>+</sup> and transferred to the positive electrode. The steep voltage decline is caused by a rapid increase of the total overpotential, which is also responsible for the larger voltage jump after discharge that significantly exceeds the IR drop.

For each cycle, charge capacity, discharge capacity, Coulombic efficiency, and energy efficiency were obtained, see Fig. 2(b). In their very early lives, i.e., during the first 10 to 20 cycles, the cells show inferior performance: the charge and discharge capacities quickly decrease and the Coulombic efficiency is rather low, indicating high self-discharge of the cells. Inferior cell performance during the first  $\sim 10$ –50 cycles is a commonly observed phenomenon of LMBs [5,10,11,16] and was attributed to impurities and side reactions [16]. In the present system with the molten salt electrolyte LiCl–NaCl–KCl (61-3-36 mol%), in particular exchange reactions between the Na metal and the foreign ions (here Li<sup>+</sup> and K<sup>+</sup>) of the molten salt are expected to occur, i.e.,  $Na + LiCl \leftrightarrow NaCl + Li$  and  $Na + KCl \leftrightarrow NaCl + K$  [9]. Such exchange reactions take place only in multi-cationic electrolytes and lead to a composition change of both the electrolyte and the negative electrode. For a small test system with 0.72 g Na and 2.67 g molten salt LiCl–NaCl–KCl (61-3-36 mol%), the exchange reactions were found to reach thermodynamic equilibrium in less than an hour and the respective equilibrium constants could be determined [9]. Based on these data, we expect an increase of the NaCl concentration in the electrolyte to 4–8 mol% and a Li concentration of 9–17 mol% in the electrode, depending on the total amounts of Na and molten salt used in the cells. Inductively coupled plasma optical emission spectroscopy (ICP-OES) indeed confirmed an increase of NaCl content in the molten salt after operation at the expense of a decreased LiCl content.

After cell initialization, i.e., once equilibrium of the side reactions is reached, stable operation is observed in the charge-discharge cycling tests: charge and discharge capacities are back at high values and the Coulombic efficiency is typically  $>99$  %, indicating a very low self-discharge current.

### 3.2. Self-discharge current

The average self-discharge current of various Na-LMB cells was determined via  $\int I_{sd}(t) dt = Q_{ch} - Q_{disc}$  from the charge and discharge capacity obtained in the GCPL tests. Hereby, cycles with strong variations in the charge/discharge capacity from cycle to cycle (as for instance observed during cell initialization) were excluded from the analysis. Additionally, the charge capacity was related with both the subsequent discharge capacity and the preceding discharge capacity to determine the involved uncertainty. The self-discharge current is found to be very stable, even for aged cells. Respective results of the average self-discharge current are summarized in Fig. 3. Slightly different values are found for each cell, with the variation from cell to cell exceeding the uncertainty of the values of each cell of up to 2 mA. Firstly, there seems to be a systematic dependence on the distance between the two electrodes, cf. Fig. 3(a). Cells with an electrode distance around 14 mm show a generally lower self-discharge current than cells with 11 mm distance. Self-discharge of the foam-less cell with 21 mm distance (cell FL2) seems

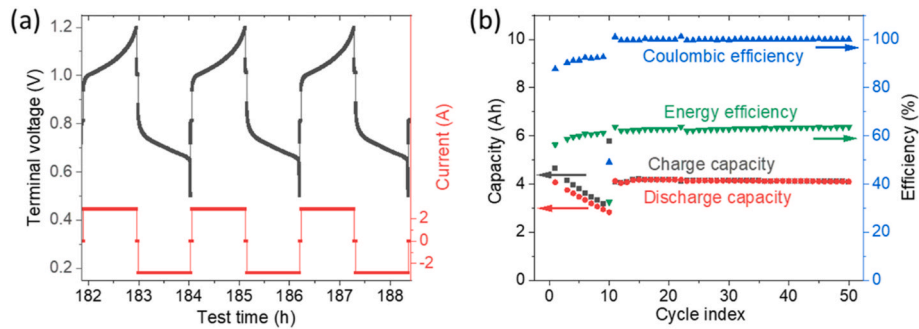


Fig. 2. Typical charge-discharge cycles of GCPL test (a) and cycle parameters (b) of cell with default design. The voltage limits (a) are 0.5 and 1.2 V, the nominal capacity (b) is 5.9 Ah.

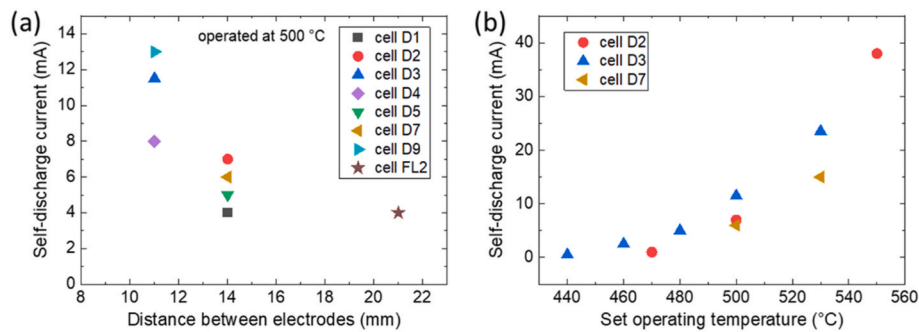


Fig. 3. Self-discharge current of various LMB test cells, plotted versus (a) the distance between the two electrodes and (b) the set operating temperature. The actual temperature of the electrolyte is about 70 K below the set operating temperature (see chapter 2. Materials and Methods).

further reduced. Secondly, there is a distinct trend regarding the temperature dependence: the higher the operating temperature of the cell the higher the self-discharge current, cf. Fig. 3(b). Both observations agree with the expectation, since self-discharge is caused by the finite solubility of Na metal in the molten salt electrolyte, which increases with temperature [17]. The resulting sodium concentration gradient in the electrolyte leads to a continuous transport of Na from the negative to the positive electrode by diffusion, which is lower for a larger distance between the electrodes.

From the self-discharge current  $I_{sd}$  respectively its density  $j_{sd} = I_{sd}/S$  with  $S$  the effective cross section area of the electrolyte, the solubility of Na metal in the electrolyte can be estimated using  $j_{sd} = FDc_{Na,s}/d$ . Here,  $F$  is the Faraday constant,  $D$  is the diffusion constant of Na metal in the electrolyte, and  $d$  is the distance between the electrodes. With  $D \approx 10^{-4} \text{ cm}^2/\text{s}$  [18], a Na solubility of  $c_{Na,s} \approx 4.4 \cdot 10^{-5} \text{ mol}/\text{cm}^3$  respectively 0.12 mol% results, which agrees with previous measurements of the solubility of Na metal in the molten salt mixture LiCl–NaCl–KCl (59-5-36 mol%) of 0.09 mol% at 450 °C [10].

### 3.3. Ohmic overpotential

The ohmic overpotential  $\eta_{ohm} = R_0 I$  was determined from the measured IR drop at switching on/off charging/discharging currents during GCPL tests (except for the voltage jump after discharge, see Fig. 2 and corresponding text). It is found that the respective resistance  $R_0$  is independent of the current and of the cell's state of charge. It attains a constant value in the operation regime after cell initialization, which depends on the geometry of the cell: cells with larger distance  $d$  between the electrodes show a higher resistance. It is reasonable to assume that the resistivity  $\rho$  of the molten salt electrolyte caused by the finite ionic conductivity  $\sigma = 1/\rho$  of the electrolyte contributes to the total ohmic resistance of the cell:  $R_0 = R_s + R_{el}$  with  $R_{el} = \rho \cdot d/S$ . Here,  $d$  is the distance between the electrodes,  $S$  is the effective cross section area of the electrolyte,  $R_{el}$  is the electrolyte's contribution to the resistance and

$R_s$  summarizes other contributions, e.g., contact resistances. As shown in Fig. 4, the data of  $R_0$  for different cells indeed fall on a straight line when plotted against  $d/S$ . Fit parameters are  $R_s = 10 \text{ m}\Omega$  and  $\rho = 0.62 \Omega \cdot \text{cm}$ , where the latter corresponds to an ionic conductivity of 1.6 S/cm. Thus, the resistance of the electrolyte is larger than the contact resistances.

According to literature [19], the total conductivity of LiCl–NaCl–KCl (55.77-3.84-40.39 mol%), a composition close to the electrolyte in the investigated cells, is  $\sigma_{total} = 3.80334 \text{ S}/\text{cm} + 0.007595 \text{ S}/(\text{cm} \cdot \text{K}) \cdot T$ . At 430 °C, the average actual temperature of the electrolyte at a set operating temperature of 500 °C, this yields a conductivity of 1.54 S/cm, which agrees very well with the value of 1.6 S/cm determined from the cycling tests.

### 3.4. Rate capability

To investigate the rate capability of the Na-LMB tests cells, GCPL tests were performed at different current densities. Fig. 5 shows

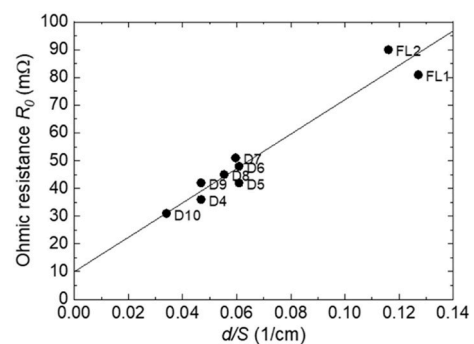


Fig. 4. Ohmic resistance  $R_0$  of various cells plotted as function of  $d/S$ , i.e., the distance between the electrodes divided by the electrolyte cross-section area. All cell tests were performed at the default set temperature of 500 °C.

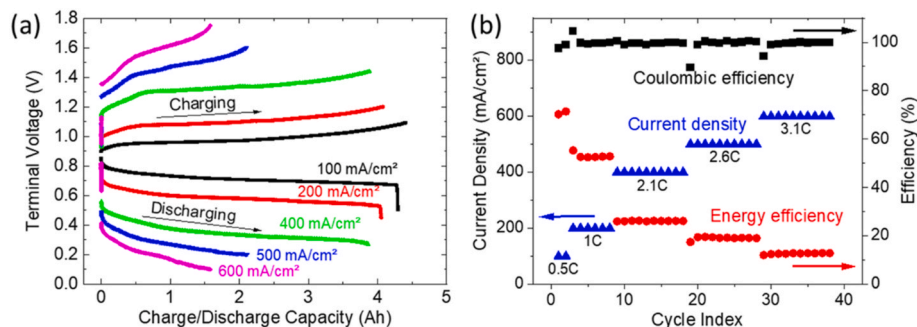


Fig. 5. GCPL tests at different current densities. (a) Measured terminal voltage versus charge respectively discharge capacity, (b) Coulombic efficiency and energy efficiency of respective charge-discharge cycles.

exemplarily the results for cell D10 with default design. As the current density increases, the overpotentials increase and the achieved charge/discharge capacity decreases. Note that the maximum achievable capacities were not reached here, because the voltage limits were not optimized for maximum utilization of Na. Nevertheless, the effect of current density on the cell performance becomes obvious. As expected, the energy efficiency decreases for increasing current density due to the larger overpotentials at higher current. The Coulombic efficiency, however, remains stably at values between 99 and 100 %. Exceptions are obtained for the first cycles with new parameters (current and voltage limits). As reference, the used currents are also given in units of the nominal cell capacity (C-rate).

In order to optimize the rate capability of the cell, the distance between the electrodes might be reduced. This is expected to lower the ohmic overpotential, which represents the main contribution to the total overpotential of the cell. Even without optimization, a current density of 600 mA/cm<sup>2</sup> could be demonstrated.

### 3.5. Cell voltage

To determine the electrochemical potential of the Na//SbBi<sub>9</sub> system, GITT measurements were performed with different cells after cell initialization, see the example of cell D7 shown in Fig. 6.

After each current pulse, the cell is allowed to relax until all overpotentials are negligible. The measured voltage at the end of each relaxation step is plotted in Fig. 7(a) versus the cell's state of charge  $SOC(t) = SOC_0 + \int I(t)dt$ . Hereby, a reasonable guess was used for the unknown initial state of charge  $SOC_0$ . Obviously, the data of the discharge pulses do not coincide with the data of the preceding charge pulses when the self-discharge of the cell is neglected. Assuming an appropriate continuous self-discharge with constant current, however, the data of consecutive charge and discharge pulses collapse on a single line. The respective values of average self-discharge current required to achieve this coincidence are slightly different for each cell and increase with temperature. They are in the range 8–15 mA at 500 °C and 17–30 mA at 530 °C. These data are consistent with the results determined

from charge-discharge cycling tests, Fig. 3.

In a next step, from the cell's SOC the concentration of Na in the Na–Sb–Bi alloy was calculated, which makes the cell voltage data independent of the individual cell geometry, in particular of the amount of Sb–Bi alloy. Fig. 7(b) shows the correlation between electrochemical potential  $U_0$  and molar concentration of Na in the Na–Sb–Bi alloy,  $x_{Na}$ , after adjusting the initial state of charge  $SOC_0$  appropriately. Except for some minor deviations observed between charging and discharging for  $x_{Na} > 0.2$  (Na contents that can be reached in foam-less cells only), data of different cells are found to collapse on a single curve, no matter which cell design was chosen (default design with foam or foam-less design), at which temperature the cells were operated, or at which cell age the data were taken (the operation times prior to GITT data acquisition ranged from 50 h to 750 h). Also added to Fig. 7(b) are data adapted from Ref. [10] for the systems Na//SbBi<sub>9</sub> and Na//Bi obtained in a specific coulometric titration device with the molten salt electrolyte LiCl–NaCl–KCl (55–9–36 mol%). According to the authors, the higher voltage for SbBi<sub>9</sub> in the initial stage of titration might be attributed to the higher voltage of the Na–Sb couple [10]. The data of the present study generally coincide with the data reported in literature. Responsible for the small differences might be the time scale of the measurement or the exchange reactions discussed above, which make the system dependent on the salt composition and on the amounts of active materials used.

### 3.6. Long-term behavior

#### 3.6.1. Amount of electrolyte

The long-term behavior of various cells was tested by charge-discharge cycling. Here, both GCPL tests with constant-current (CC) charging and constant-current constant-voltage (CCCV) charging were applied. Fig. 8 shows the cycle statistics of two test cells with different amounts of electrolyte, cell D4 with 120 g molten salt and cell D10 with 150 g salt. Cell D4 was run with CCCV charging for 550 cycles at 2.83 A (100 mA/cm<sup>2</sup>) and cell D10 was run with CC charging for 750 cycles at 5.65 A (200 mA/cm<sup>2</sup>). For both cells, the Coulombic efficiency remains stably at a value > 99 % over the entire duration of the test, while the

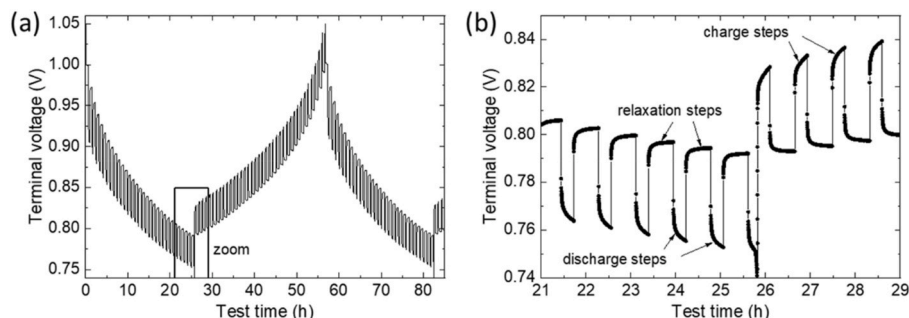
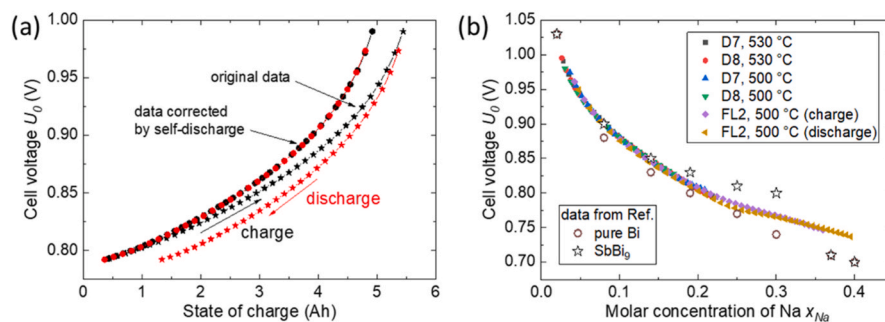
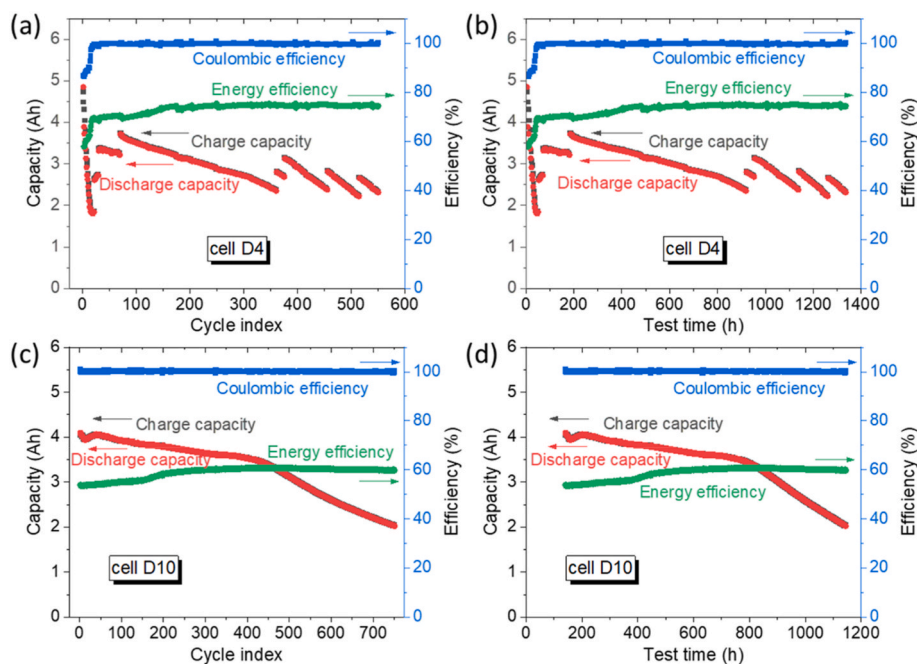


Fig. 6. Example of GITT data (cell D7): Charging/discharging currents of  $\pm 0.5$  A were applied for 1000 s, followed by 2000 s of relaxation.



**Fig. 7.** Cell voltage as function (a) of SOC for cell D7 (set temperature 530 °C) and (b) of molar concentration of Na in the positive electrode Sb–Bi–Na alloy for different cells and at different set temperatures. Literature data are taken from Ref. [10].



**Fig. 8.** Long-term charge-discharge cycling tests of cell D4 (120 g electrolyte, (a),(b)) and cell D10 (150 g electrolyte, (c),(d)). Cell performance as function of cycle index (a),(c) and versus test time (b),(d). Cell D10 was used for other tests prior to the GCPL test.

energy efficiency slightly increases with cell age (see discussion below). The different levels of energy efficiency stem from the different currents used for cycling (see also Fig. 5).

Despite the good cycling performance, the charge and discharge capacities of both cells decrease with cell age. Compared with cells that contained a lower amount of electrolyte (cell D4), cells with higher amount of electrolyte (cell D10) show a slower capacity decrease in the first ~800 h. In addition, only cell D4 shows a capacity that jumps back from time to time to a higher value. Both observations can be explained by continuous evaporation of Na into the empty space above the electrolyte, its condensation at the colder cover, and subsequent dropping back when a critical drop size is reached. In cell D4, the metal foam with Na was covered by 8 mm of molten salt electrolyte, while in cell D10 the level of molten salt was 17 mm above the metal foam. Similar to self-discharge, where a larger distance between the electrodes reduced the transport of dissolved Na to the positive electrode, also the transport of dissolved Na to the free electrolyte surface and its subsequent evaporation is reduced when the thickness of the electrolyte above the negative electrode is increased. This explains the lower capacity loss of cell D10 during the first ~800 h. During cell disassembly, Na droplets were indeed found attached at the cell cover of both cells, which confirms evaporation and condensation of Na. A typical photograph shows

numerous tiny droplets (less than 1 mm) and 10 bigger drops, 6–9 mm in diameter and up to 2 mm in height. This amounts to a total volume of about 1.1 cm<sup>3</sup>, corresponding to a capacity of 1.3 Ah, which is in reasonable agreement with the observed capacity loss in the first ~800 h. The accelerated capacity decrease after ~800 h of operation cannot be explained by evaporation; it might be related with corrosion of solid cell components.

### 3.6.2. Influence of PCC material

The strongest corrosion attack on solid cell components is expected for the positive current collector (PCC) made of SS 316Ti (cell body), which is in direct contact with the liquid metal alloy  $SbBi_9$  of the positive electrode. In order to evaluate the potential influence of corrosion on the cell performance, a cell with Mo as PCC was built and tested (called cell M1). A Mo crucible was placed inside the cell body, into which the positive electrode was filled. This reduced the surface area of the positive electrode from 28.3 to 24.5 cm<sup>2</sup>. All other design and cycling criteria were adapted from cell D10, i.e., design with foam, same distance between electrodes, same amount of electrolyte, CC cycling with 200 mA/cm<sup>2</sup>. Because the same current density was used for cycling, the lower current (proportional to surface area) used for cell M1 is expected to compensate the higher resistance (inversely proportional to surface

area), thus resulting in the same energy efficiency. Fig. 9 compares the cycling performance of cell M1 with the previously shown results of cell D10. Indeed, the energy efficiency of M1 is quite similar to that of cell D10 at the beginning of the cycling test. In contrast to the increasing energy efficiency observed for D10 and all other cells with a PCC made of stainless steel, however, the energy efficiency of cell M1 stays constant. At  $\sim 800$  h, a sudden increase of the self-discharge current of cell M1 is observed, which is attributed to the design using a non-perfectly fitting crucible. Irrespective of the high self-discharge, the charge and discharge capacities do not show an accelerated decrease after 800 h as was observed for all previous cells with SS 316Ti as PCC. Instead, the moderate capacity decrease continues and even declines, which is the expected trend for loss of active Na due to evaporation.

For a better understanding of energy efficiency increase and cell capacity decrease, the individual charge-discharge cycles are compared. In Fig. 10, GCPL test data of the two cells D10 and M1 are shown, where the measured terminal voltage is plotted versus the degree of discharge  $DOD = Q_{nom} / SOC$ . Hereby, the initial DOD of each presented cycle is adjusted so that the final voltage in the relaxation step after charging matches the cell voltage curve obtained from GITT data, Fig. 7(b).

For cell D10, the voltage curves measured during charging and discharging show a symmetric change within the first  $\sim 700$  h of operation, indicating a decrease in total overpotential, while the cell voltage remains stable during the entire test. After  $\sim 700$  h, no further changes in overpotential are observed; except for a decreasing cell capacity, the curves fall on each other. The observed decrease in overpotential during the first  $\sim 700$  h was also observed for the other cells with the PCC made of SS 316Ti and results in the previously mentioned increase of energy efficiency, see Fig. 8. In contrast to the significant decrease in overpotential and increase in energy efficiency just described, cell M1 with Mo as positive current collector shows much more stable voltage curves during cycling and a much more stable overpotential, see Fig. 10(b). Consequently, the energy efficiency does not increase but remains at a constant value during cycling (Fig. 9).

Similar behavior is reported in literature for Li-LMBs. During cycling tests of a Li//Sb<sub>2</sub>Sn<sub>6</sub> cells, a significant overpotential decrease was observed between the 3rd and 20th cycle when stainless steel SS304 was used as PCC material [11]. The same cell using a PCC made of molybdenum showed a less pronounced but still clearly visible overpotential decrease from the 10th to the 100th cycle, while a stable overpotential was observed when tungsten was used as PCC [20]. Corrosion investigations showed very strong attack of SS304 by the Li-Sb-Sn alloy, strong attack of Mo, and mild attack of W [11,20]. The corrosion attack of PCC materials by the Na-Sb-Bi alloy used in the present study was found to be much milder than the attack by Li-Sb-Sn, see Fig. 11. After 1335 h of operation, the stainless steel 316Ti shows an attack of up to 50  $\mu$ m depth with strong depletion of Fe, Cr, and Ni and severe penetration of Sb and Bi, while no attack is visible on Mo after 1200 h of operation.

From all these observations, both our own and the ones found in

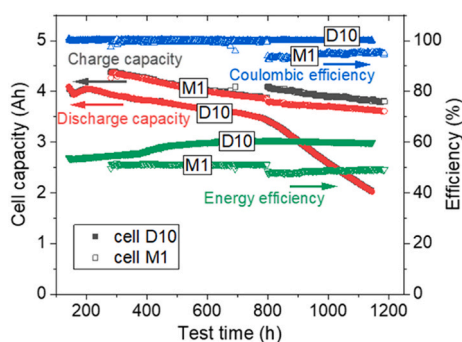


Fig. 9. Long-term cycling behavior of cell D10 (SS 316Ti as PCC) and cell M1 (Mo as PCC) as function of test time. Both cells were used for other tests prior to the GCPL test.

literature, it can be concluded that the decrease in total overpotential and the corresponding increase in energy efficiency is related with corrosion of the PCC material, although a reasonable explanation of this relation is hitherto lacking.

Regarding the capacity loss, both cells show a stable SOC reached after charging, while the maximum achievable DOD after discharge decreases with cell age. Since the lower voltage limit of the charge-discharge cycles was set such that all available Na is transferred to the positive electrode upon discharge, this clearly indicates a loss in available active Na. Active Na may be lost or inactivated by evaporation as discussed above or by chemical reactions that permanently bind Na. Since evaporation is expected to be similarly pronounced for cell D10 and cell M1 (same level of molten salt above metal foam) and not to increase but rather to decline during operation, it explains the capacity loss observed for cell M1 during the entire test, but for cell D10 only in the first  $\sim 800$  h. The accelerated capacity loss of cell D10 after 800 h must be caused by a process not present in cell M1, e.g., corrosion of SS 316Ti by the positive electrode. In contrast to Mo, which does not form intermetallic phases with Sb or Bi, steel alloying elements such as Fe, Cr, and Ni are dissolved into the liquid Na-Sb-Bi alloy during cell operation and form intermetallic phases with Sb and/or Bi, for instance FeSb<sub>2</sub>, FeSb, CrSb<sub>2</sub>, CrSb, NiSb<sub>2</sub>, NiBi<sub>3</sub> [21]. Hereby, only the compounds FeSb<sub>2</sub> and CrSb<sub>2</sub> (respectively the solid solution (Fe,Cr)Sb<sub>2</sub>) are formed from the very beginning of the corrosion process due to the insignificant solubility of Fe and Cr in both Sb and Bi [22,23]. The formation of the other compounds requires threshold concentrations of Fe, Cr, and Ni (Ni has a rather high solubility of about 10 mol% in Bi), which might be reached in a later stage of corrosion. The expected decrease in active Sb and Bi due to the formation of corrosion products is insignificant because of the rather high initial amount of Sb-Bi alloy in the cells, which is confirmed by the stable cell voltage, see Fig. 10. However, the intermetallic phases might influence the alloying process of Na with SbBi<sub>9</sub>. In the Sb-Bi alloy, the Sb is not freely available for reactions with Na. The Fe-Sb and Cr-Sb corrosion products might make the Sb more easily accessible for reactions with Na. This could have two effects. Firstly, the alloying process between Na and Sb occurs more easily, which results in a reduced activation overpotential and explains the observed decrease in total overpotential and increase in energy efficiency during the first  $\sim 700$  h of operation (see Figs. 8, 9, and 10). Secondly, also the formation of solid Na-compounds (Na<sub>3</sub>Sb, Na<sub>3</sub>Bi) is facilitated, which finally decreases the amount of Na available for charge-discharge cycling and reduces the cell capacity. The formation of Na-compounds might require either a certain concentration of corrosion products or specific compounds that are formed in a later stage. This could explain that no effect of corrosion on the cell capacity is observed in the first  $\sim 800$  h. However, further research is required to clarify the interaction between corrosion products and Na alloying.

#### 4. Conclusion

Na//SbBi<sub>9</sub> liquid metal batteries with molten salt electrolyte LiCl-NaCl-KCl (61-3-36 mol%) and different cell designs, one design including a metal foam that hosts the liquid Na and the other design without a metal foam, could be realized and successfully operated. Stable operation with excellent electrochemical performance was demonstrated after a short time of cell initialization. The self-discharge current is only  $\sim 0.35$  mA/cm<sup>2</sup> and depends on operating temperature and electrode distance in a reasonable way. The main contribution to the ohmic resistance stems from the electrolyte, while the contact resistances sum up to only 10 m $\Omega$ . The cell voltage was found to be independent of cell design, operating temperature, and cell age. In long-term cycling tests, the cells show a stable Coulombic efficiency and energy efficiency, the latter even slightly increasing when stainless steel is used as positive current collector. However, the cell capacity of all cells decreases due to a loss in active sodium. Two mechanisms could be identified. First of all, Na evaporates into the empty space of the cell, an

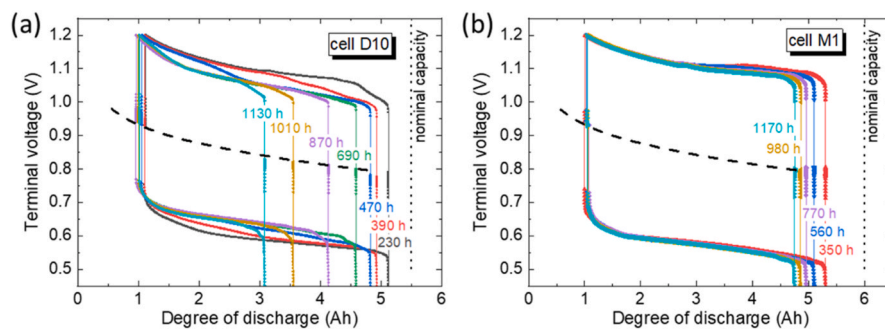


Fig. 10. Selected cycles of GCPL tests of cell D10 (a) and cell M1 (b) plotted versus the respective degree of discharge. The dashed lines represent the cell voltage  $U_0$  as determined from GITT data. The data of cell M1 collected after 800 h were self-discharge-corrected.

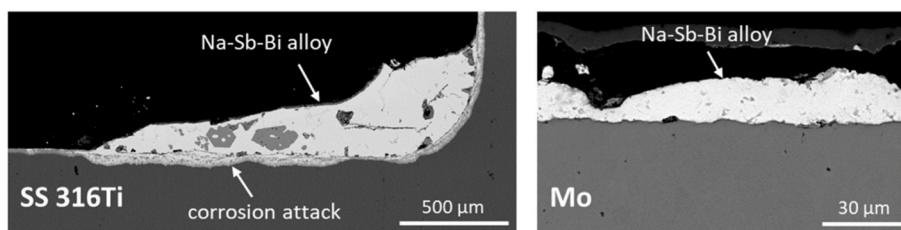


Fig. 11. Scanning electron microscopy (backscattered electron) images of cross sections of different PCC materials after cell operation.

effect influenced by the amount of electrolyte. Secondly, corrosion of stainless steel by the positive electrode leads to an additional capacity loss not observed when molybdenum is used as positive current collector. The results obtained in the present study form the basis for future cell optimization and upscaling.

#### CRedit authorship contribution statement

**Renate Fetzer:** Investigation, Writing – original draft. **Tianru Zhang:** Investigation. **Florian Lindner:** Investigation. **Alfons Weisenburger:** Conceptualization, Writing – review & editing. **Georg Müller:** Conceptualization, Funding acquisition.

#### Declaration of competing interest

The authors declare that they have no known competing financial interests or personal relationships that could have appeared to influence the work reported in this paper.

#### Data availability

Data will be made available on request.

#### Acknowledgments

The salt compositions were determined using ICP-OES at the Institute of Applied Materials (IAM-AWP) at KIT. The authors acknowledge fruitful discussions with Kangli Wang and Wenjin Ding. The authors are grateful to the Deutsche Forschungsgemeinschaft (DFG) and National Natural Science Foundation of China (NSFC) for funding the DFG-NSFC Sino-German Project (DFG Project Number 411450529): “Study on Corrosion Control and Low-Temperature Electrolytes for Low-Cost Na-based Liquid Metal Batteries”.

#### References

- [1] H. Kim, D.A. Boysen, J.M. Newhouse, B.L. Spatocco, B. Chung, P.J. Burke, D. J. Bradwell, K. Jiang, A.A. Tomaszowska, K. Wang, W. Wei, L.A. Ortiz, S.A. Barriga,

- S.M. Poizeau, D.R. Sadoway, Liquid metal batteries: past, present, and future, *Chem. Rev.* 113 (2013) 2075–2099, <https://doi.org/10.1021/cr300205k>.
- [2] H. Li, H. Yin, K. Wang, S. Cheng, K. Jiang, D.R. Sadoway, Liquid metal electrodes for energy storage batteries, *Adv. Energy Mater.* 6 (2016), <https://doi.org/10.1002/aenm.201600483>.
- [3] K. Wang, K. Jiang, B. Chung, T. Ouchi, P.J. Burke, D.A. Boysen, D.J. Bradwell, H. Kim, U. Muecke, D.R. Sadoway, Lithium-antimony-lead liquid metal battery for grid-level energy storage, *Nature* 514 (2014) 348–350, <https://doi.org/10.1038/nature13700>.
- [4] H. Li, K. Wang, S. Cheng, K. Jiang, High performance liquid metal battery with environmentally friendly antimony-tin positive electrode, *ACS Appl. Mater. Interfaces* 8 (2016) 12830–12835, <https://doi.org/10.1021/acsami.6b02576>.
- [5] K. Cui, P. Li, W. Zhao, C. Liu, S. Li, D. Zhou, X. Qu, Self-healing action of Bi in high-performance Sb–Bi–Sn positive electrodes for liquid metal batteries, *J. Power Sources* 538 (2022), 231584, <https://doi.org/10.1016/j.jpowsour.2022.231584>.
- [6] D.J. Bradwell, H. Kim, A.H.C. Sirk, D.R. Sadoway, Magnesium-antimony liquid metal battery for stationary energy storage, *J. Am. Chem. Soc.* 134 (2012) 1895–1897, <https://doi.org/10.1021/ja209759s>.
- [7] T. Ouchi, H. Kim, X. Ning, D.R. Sadoway, Calcium-antimony alloys as electrodes for liquid metal batteries, *J. Electrochem. Soc.* 161 (2014) A1898, <https://doi.org/10.1149/2.0801412jes>.
- [8] E.J. Cairns, C.E. Crouthamel, A.K. Fischer, M.S. Foster, J.C. Hesson, C.E. Johnson, H. Shimotake, A.D. Tevebaugh, Galvanic Cells with Fused-Salts Electrolytes, ANL-7316, Illinois, USA, 1967, <https://doi.org/10.2172/4543889>.
- [9] W. Ding, Q. Gong, S. Liang, R. Hoffmann, H. Zhou, H. Li, K. Wang, T. Zhang, A. Weisenburger, G. Müller, A. Bonk, Multi-cationic molten salt electrolyte of high-performance sodium liquid metal battery for grid storage, *J. Power Sources* 553 (2023), 232254, <https://doi.org/10.1016/j.jpowsour.2022.232254>.
- [10] H. Zhou, H. Li, Q. Gong, S. Yan, X. Zhou, S. Liang, W. Ding, Y. He, K. Jiang, K. Wang, A sodium liquid metal battery based on the multi-cationic electrolyte for grid energy storage, *Energy Storage Mater.* 50 (2022) 572–579, <https://doi.org/10.1016/j.ensm.2022.05.032>.
- [11] K. Cui, F. An, W. Zhao, P. Li, S. Li, C. Liu, X. Qu, Feasibility research of SS304 serving as the positive current collector of Li||Sb–Sn liquid metal batteries, *J. Phys. Chem. C* 125 (2021) 237–245, <https://doi.org/10.1021/acs.jpcc.0c09629>.
- [12] W. Liu, H. Yin, K. Du, B. Yang, D. Wang, Corrosion behaviors of iron, chromium, nickel, low-carbon steel, and four types of stainless steels in liquid antimony-tin alloy, *Corrosion* 77 (2021) 1192–1202, <https://doi.org/10.5006/3820>.
- [13] T. Emmerich, C. Schroer, Corrosion in austenitic steels and nickel-based alloys caused by liquid tin at high temperature, *Corrosion Sci.* 120 (2017) 171–183, <https://doi.org/10.1016/j.corsci.2017.02.025>.
- [14] A. Heinzl, A. Weisenburger, G. Müller, Corrosion behavior of austenitic steel AISI 316L in liquid tin in the temperature range between 280 and 700 °C, *Mater. Corros.* 68 (2017) 831–837, <https://doi.org/10.1002/maco.201609211>.
- [15] T. Dai, Y. Zhao, X.H. Ning, R. Lakshmi Narayan, J. Li, Z. wei Shan, Capacity extended bismuth-antimony cathode for high-performance liquid metal battery, *J. Power Sources* 381 (2018) 38–45, <https://doi.org/10.1016/j.jpowsour.2018.01.048>.
- [16] S. Yan, X. Zhou, H. Li, Y. Shen, Y. He, H. Zhou, K. Wang, K. Jiang, Utilizing in situ alloying reaction to achieve the self-healing, high energy density and cost-effective

- Li||Sb liquid metal battery, *J. Power Sources* 514 (2021), 230578, <https://doi.org/10.1016/j.jpowsour.2021.230578>.
- [17] M.A. Bredig, J.W. Johnson, W.T. Smith, Miscibility of liquid metals with salts. I. The sodium-sodium halide systems, *J. Am. Chem. Soc.* 77 (1955) 307–312, <https://doi.org/10.1021/ja01607a016>.
- [18] A.Z. Borucka, J.O. Bockris, J.A. Kitchener, Self-diffusion in molten sodium chloride: a test of the applicability of the Nernst–einstein equation, *Proc. Math. Phys. Eng. Sci.* 241 (1957) 554–567, <https://doi.org/10.1098/rspa.1957.0146>.
- [19] G.J. Janz, C.B. Allen, N.P. Bansal, R.M. Murphy, R.P.T. Tomkins, *Physical Properties Data Compilations Relevant to Energy Storage. II. Molten Salts: Data on Single and Multi-Component Salt Systems*, United States, 1979. <https://www.osti.gov/biblio/6302819>.
- [20] K. Cui, W. Zhao, D. Zhou, S. Li, C. Liu, P. Li, X. Qu, Stable positive current collectors for Li||Sb–Sn liquid metal batteries, *ACS Appl. Energy Mater.* 4 (2021) 9013–9021, <https://doi.org/10.1021/acsaem.1c01280>.
- [21] H. Okamoto, M.E. Schlesinger, E.M. Mueller (Eds.), *ASM Handbook, Volume 3: Alloy Phase Diagrams*, ASM International, 2016, <https://doi.org/10.31399/asm.hb.v03.9781627081634>.
- [22] D. Boa, S. Hassam, G. Kra, K.P. Kotchi, J. Rogez, The ternary bismuth–iron–antimony system: experimental phase diagram study and thermodynamic evaluation, *Calphad* 32 (2008) 227–239, <https://doi.org/10.1016/j.calphad.2008.01.001>.
- [23] Y. Xia, Y. Liu, C. Wu, H. Peng, H. Tu, J. Wang, X. Su, 650 and 750 °C isothermal sections of the Cr–Sb–Fe system, *J. Phase Equilibria Diffus.* 39 (2018) 426–436, <https://doi.org/10.1007/s11669-018-0653-0>.